

THE DYNAMICAL STATE OF FILAMENTARY INFRARED DARK CLOUDS

AUDRA K. HERNANDEZ

Department of Astronomy, University of Florida, Gainesville, FL 32611, USA;
 audrah@astro.ufl.edu

JONATHAN C. TAN

Departments of Astronomy & Physics, University of Florida, Gainesville, FL 32611, USA;
 jt@astro.ufl.edu

Draft version January 11, 2011

ABSTRACT

The dense, cold gas of Infrared Dark Clouds (IRDCs) is thought to be representative of the initial conditions of massive star and star cluster formation. We analyze $^{13}\text{CO } J = 1 - 0$ line emission data from the Galactic Ring Survey of Jackson et al. for two filamentary IRDCs, comparing the mass surface densities derived from ^{13}CO , $\Sigma_{13\text{CO}}$, with those derived from mid-infrared small median filter extinction mapping, Σ_{SMF} , by Butler & Tan. After accounting for molecular envelopes around the filaments, we find approximately linear relations between $\Sigma_{13\text{CO}}$ and Σ_{SMF} , i.e. an approximately constant ratio $\Sigma_{13\text{CO}}/\Sigma_{\text{SMF}}$ in the clouds. There is a variation of about a factor of two between the two clouds. We find evidence for a modest decrease of $\Sigma_{13\text{CO}}/\Sigma_{\text{SMF}}$ with increasing Σ , which may be due to a systematic decrease in temperature, increase in importance of high ^{13}CO opacity cores, increase in dust opacity, or decrease in ^{13}CO abundance due to depletion in regions of higher column density. We perform ellipsoidal and filamentary virial analyses of the clouds, finding that the surface pressure terms are dynamically important and that globally the filaments may not yet have reached virial equilibrium. Some local regions along the filaments appear to be close to virial equilibrium, although still with dynamically important surface pressures, and these appear to be sites where star formation is most active.

Subject headings: ISM: clouds, dust, extinction — stars: formation

1. INTRODUCTION

Massive, high column density Infrared Dark Clouds (IRDCs), typically identified as being opaque against the Galactic background at $\sim 10\mu\text{m}$, are thought to contain the sites of future massive star and star cluster formation (e.g. Rathborne et al. 2006), since their densities ($n_{\text{H}} \gtrsim 10^4 \text{ cm}^{-3}$) and mass surface densities ($\Sigma \gtrsim 0.1 \text{ g cm}^{-2}$) are similar to regions known to be undergoing such formation activity (Tan 2007). Studies of molecular line emission from IRDCs can help determine their kinematics. In particular, we would like to know if they are gravitationally bound, if they are near virial equilibrium and if there is evidence for coherent gas motions that might indicate that IRDC formation involves converging atomic flows (Heitsch et al. 2008) or converging molecular flows from cloud collisions (Tan 2000).

In this study we use $^{13}\text{CO } J = 1 - 0$ line emission data from the Galactic Ring Survey (GRS) (Jackson et al. 2006) for two filamentary IRDCs, clouds F ($l = 34.437^\circ$, $b = 0.245^\circ$, $d = 3.7 \text{ kpc}$) and H ($l = 35.395^\circ$, $b = -0.336^\circ$, $d = 2.9 \text{ kpc}$) from the sample of 10 relatively nearby massive and dense IRDCs of Butler & Tan (2009, hereafter BT09), comparing ^{13}CO -derived mass surface densities, $\Sigma_{13\text{CO}}$, with small median filter (SMF) mid-infrared (MIR) ($8\mu\text{m}$) extinction mapping derived mass surface densities, Σ_{SMF} , using the method of BT09 applied to the *Spitzer* Infrared Array Camera (IRAC) band 4 images of the Galactic plane taken as part of the Galactic Legacy Mid-Plane Survey Extraordinaire (GLIMPSE) (Benjamin et al. 2003). We consider systematic errors in each of these methods, which is necessary before analyzing larger samples of clouds. We are also able to look for evidence of changing CO abundance with column density, e.g. due to possible depletion of CO at high densities. We then perform a virial analysis of the clouds to determine their dynamical state.

There have been a number of other studies comparing ^{13}CO derived mass surface densities with those from other methods. For example, Goodman, Pineda & Schnee (2009) compared near infrared (NIR) dust extinction, far infrared (FIR) dust emission and ^{13}CO line emission in the Perseus giant molecular cloud (GMC), probing values of Σ up to $\sim 0.02 \text{ g cm}^{-2}$ (i.e. up to $A_V \simeq 8 \text{ mag}$). Even after accounting for temperature and optical depth variations they concluded that ^{13}CO emission was a relatively unreliable tracer of mass surface density, perhaps due to threshold, depletion and opacity effects. Our study probes higher values of Σ , from ~ 0.01 to $\sim 0.05 \text{ g cm}^{-2}$, and compares ^{13}CO emission with MIR extinction in order to investigate these processes.

Battersby et al. (2010) used ^{13}CO emission, MIR extinction and FIR dust emission methods to measure Σ and mass of clumps in 8 IRDCs, one of which is IRDC F of our study. They did not present a specific comparison of $\Sigma_{13\text{CO}}$ with other methods, although derived clump masses were in reasonable agreement. Their sample also included MIR-bright regions, associated with ultra-compact HII regions, for which the MIR extinction method cannot be applied. As we describe below, our approach differs in a number of ways, including by focusing on filamentary and mostly quiescent regions of IRDCs for which the MIR extinction method is most reliable and which are likely to be closer to the initial conditions of the massive star and star cluster formation process. We note that while IRDC F in particular does contain some regions

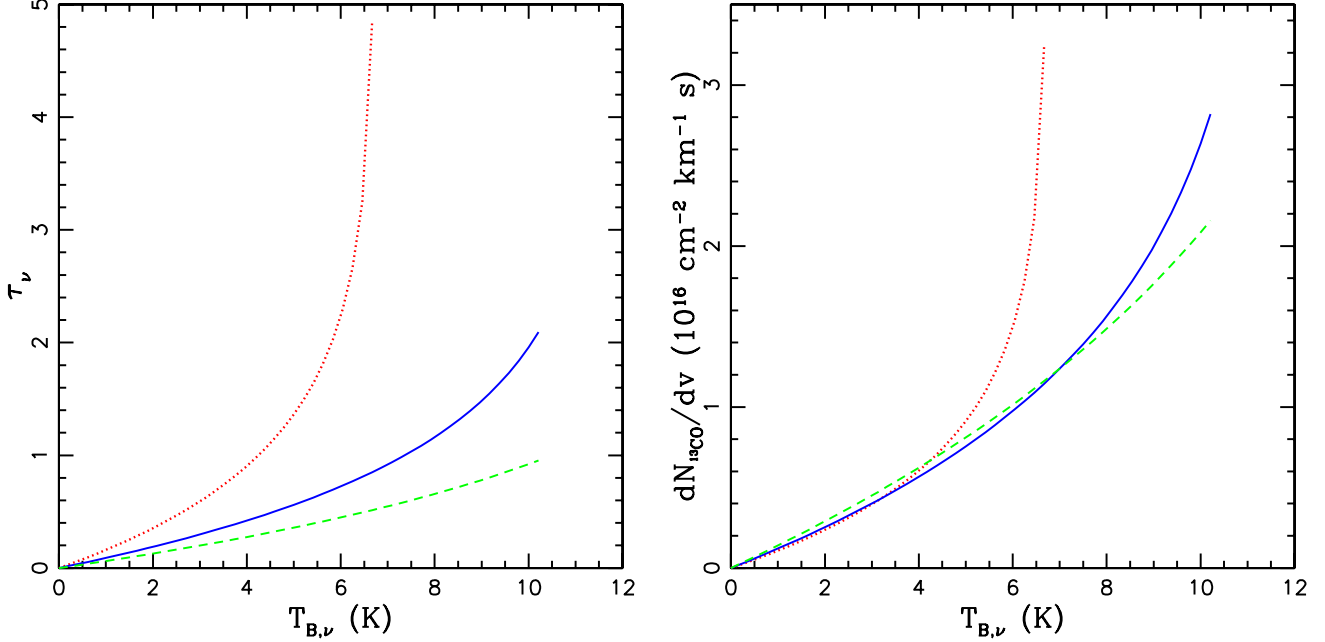


FIG. 1.— (a) Left panel: Dependence of τ_ν with $T_{B,\nu}$ (eq. 2) assuming $T_{\text{ex}} = 10, 15, 20$ K (red dotted, blue solid, green dashed lines, respectively). (b) Right panel: Dependence of $dN_{13\text{CO}}/dv$ with $T_{B,\nu}$ assuming $T_{\text{ex}} = 10, 15, 20$ K (red dotted, blue solid, green dashed lines, respectively).

of quite active star formation, including an ultra-compact H II region, here we have concentrated on its more quiescent portions.

2. MASS SURFACE DENSITY ESTIMATION FROM ^{13}CO

We evaluate the column density of ^{13}CO molecules, $dN_{13\text{CO}}$, in a velocity interval dv from their $J = 1 \rightarrow 0$ emission via

$$\frac{dN_{13\text{CO}}(v)}{dv} = \frac{8\pi Q_{\text{rot}}}{A\lambda_0^3} \frac{g_l}{g_u} \tau_\nu \left[1 - \exp\left(-\frac{h\nu}{kT_{\text{ex}}}\right) \right]^{-1}, \quad (1)$$

where Q_{rot} is the partition function, $A = 6.3355 \times 10^{-8} \text{ s}^{-1}$ is the Einstein coefficient, $\lambda_0 = 0.27204$ cm, $g_l = 1$ and $g_u = 3$ are the statistical weights of the lower and upper levels, τ_ν is the optical depth of the line at frequency ν , i.e. at velocity v , T_{ex} is the excitation temperature (assumed to be the same for all rotational levels). For linear molecules, the partition function is $Q_{\text{rot}} = \sum_{J=0}^{\infty} (2J+1) \exp(-E_J/kT_{\text{ex}})$ with $E_J = J(J+1)hB$ where J is the rotational quantum number and $B = 5.5101 \times 10^{10} \text{ s}^{-1}$ is the rotational constant. Thus for $^{13}\text{CO}(1-0)$ we have $E_J/k = 5.289$ K. For $J = 1$, $Q_{\text{rot}} = 4.134, 6.018, 7.906$ for $T_{\text{ex}} = 10, 15, 20$ K.

The optical depth is determined via

$$T_{B,\nu} = \frac{h\nu}{k} [f(T_{\text{ex}}) - f(T_{\text{bg}})] [1 - e^{-\tau_\nu}], \quad (2)$$

where $T_{B,\nu}$ is the brightness temperature at frequency ν , $f(T) \equiv [\exp(h\nu/[kT]) - 1]^{-1}$, and $T_{\text{bg}} = 2.725$ K is the background temperature. $T_{B,\nu}$ is derived from the antenna temperature, T_A , via $T_A \equiv \eta f_{\text{clump}} T_{B,\nu}$, where η is the main beam efficiency ($\eta = 0.48$ for the GRS) and f_{clump} is the beam dilution factor of the ^{13}CO emitting gas, which we assume to be 1 for the IRDCs we are studying. However, it should be noted that the BT09 MIR extinction maps of the IRDCs do show that there is structure on scales smaller than the angular resolution of the GRS survey. Given the observed $T_{B,\nu}$ and for an assumed T_{ex} we solve equations (1) and (2) for τ_ν and thus $dN_{13\text{CO}}/dv$ (see Fig. 1). For a given $T_{B,\nu}$, this figure allows us to judge the sensitivity of the derived column density per unit velocity to temperature uncertainties.

While we use the above formulae, which account for optical depth, to calculate our column density estimates, for convenience we also state their behavior in the limit of optically thin conditions. We have $T_{B,\nu} = (h\nu/k)[f(T_{\text{ex}}) - f(T_{\text{bg}})]\tau_\nu$ so that

$$\frac{dN_{13\text{CO}}(v)}{dv} = 1.242 \times 10^{14} \frac{Q_{\text{rot}}}{f(T_{\text{ex}}) - f(T_{\text{bg}})} [1 - \exp(-h\nu/kT_{\text{ex}})]^{-1} \frac{T_A/K}{\eta f_{\text{clump}}} \text{ cm}^{-2} \text{ km}^{-1} \text{ s} \quad (3)$$

$$\rightarrow 1.144 \times 10^{15} \frac{T_A/K}{\eta f_{\text{clump}}} \text{ cm}^{-2} \text{ km}^{-1} \text{ s} \quad (T_{\text{ex}} = 15 \text{ K}). \quad (4)$$

The last coefficient changes to $(0.9865, 1.347) \times 10^{15}$ for $T_{\text{ex}} = 10, 20$ K.

Devine (2009) estimates a temperature of 19 K for cloud F based on VLA observations of $\text{NH}_3(1, 1)$ and $(2, 2)$. For this cloud, we thus adopt a temperature of 20 K. For cloud H we choose a more typical IRDC temperature of 15 K (Carey et al. 1998; Carey et al. 2000; Pillai et al. 2006). We also consider the effect of varying these temperatures.

The GRS has an angular resolution of $46''$, with sampling every $22''$. The velocity resolution is 0.22 km s^{-1} (Jackson et al. 2006). From a morphological examination of the ^{13}CO emission in l, b, v space and comparison to the MIR extinction maps of BT09 we identify the velocity range of the gas associated with each IRDC filament (see Figs. 2, 3 and 4). For cloud F we consider associated gas to be at LSR velocities $48 - 65 \text{ km s}^{-1}$ and for cloud H at $40 - 50 \text{ km s}^{-1}$. The total ^{13}CO column is then evaluated over the velocity range of the cloud $N_{^{13}\text{CO}} = \int dN_{^{13}\text{CO}}$.

To convert from $N_{^{13}\text{CO}}$ to total mass surface density $\Sigma_{^{13}\text{CO}}$ we first assume

$$\frac{n_{^{12}\text{CO}}}{n_{^{13}\text{CO}}} = 6.2 \frac{R_{\text{gal}}}{\text{kpc}} + 18.7 \quad (5)$$

(Milam et al. 2005), where R_{gal} is the galactocentric radius. For clouds F and H we estimate $R_{\text{gal}} = 5.37, 5.89$ kpc, respectively (assuming $R_{\text{gal},0} = 8.0$ kpc), which would yield $n_{^{12}\text{CO}}/n_{^{13}\text{CO}} = 52, 55$, respectively. For simplicity we adopt $n_{^{12}\text{CO}}/n_{^{13}\text{CO}} = 54$ for both clouds. We then assume

$$\frac{n_{^{12}\text{CO}}}{n_{\text{H}_2}} = 2.0 \times 10^{-4}, \quad (6)$$

similar to the results of Lacy et al. (1994). The observed variation in this abundance in GMCs is about a factor of two (Pineda, Caselli, & Goodman 2008), and this uncertainty is a major contributor to the overall systematic uncertainty in our estimate of $\Sigma_{^{13}\text{CO}}$. Thus our assumed abundance of ^{13}CO to H_2 is 3.70×10^{-6} and

$$\Sigma_{^{13}\text{CO}} = 1.26 \times 10^{-2} \frac{N_{^{13}\text{CO}}}{10^{16} \text{ cm}^{-2}} \text{ g cm}^{-2}, \quad (7)$$

assuming a mass per H nucleus of $\mu_{\text{H}} = 2.34 \times 10^{-24} \text{ g}$.

The assumption of LTE breaks down if the density of the gas is lower than the effective critical density, βn_{crit} , i.e. the critical density of ^{13}CO ($J=1-0$), $n_{\text{crit}} = 1.9 \times 10^3 \text{ cm}^{-3}$, allowing for radiative trapping with escape probability $\beta = e^{-\bar{\tau}}$, where we approximate $\bar{\tau}$ as the column density weighted mean value of τ_{ν} . Note, for a spherical cloud we would set $\bar{\tau}$ equal to the average of $\tau_{\nu}/2$, but we use τ_{ν} for these clouds with a filamentary geometry since we expect τ_{ν} seen along our line of sight to be relatively small compared to other viewing angles. Heyer et al. (2009) argued sub-thermal excitation of ^{13}CO rotational levels may be common in GMCs, causing lower values of line emission than expected under LTE conditions and thus causing estimates of Σ based on LTE assumptions to be underestimates. The IRDC filaments we are considering are generally of higher density than the typical GMC volumes considered by Heyer et al. (2009). For the average and highest intensity spectra in each IRDC (see Fig. 2), we evaluate β (see Table 1). We also estimate n_{H_2} , assuming a filament line-of-sight thickness that is equal to its observed width. A comparison of n_{H_2} with βn_{crit} shows that the densities are close to or greater than the effective critical densities, thus justifying the assumption of LTE conditions. Furthermore, we expect that the typical density at a given location is greater than our estimated values due to clumping on angular scales that are smaller than the $46''$ resolution of the CO observations. Such clumping is apparent in the MIR extinction maps (Figs. 3 & 4).

3. COMPARISON $\Sigma_{^{13}\text{CO}}$ AND Σ_{SMF} : POSSIBLE TRENDS IN TEMPERATURE, CO DEPLETION AND DUST OPACITY WITH Σ

The morphologies of IRDCs F and H are shown in Figures 3 and 4, respectively. The ^{13}CO emission is more extended than the structure traced by the BT09 MIR extinction maps, which are derived by comparing the observed $8\mu\text{m}$ intensity at the cloud position with the expected background intensity interpolated from nearby regions. Uncertainties in this estimation of the background lead to a lack of sensitivity of the MIR extinction maps to mass surface density contrasts $\Delta\Sigma \lesssim 0.013 \text{ g cm}^{-2}$.

Since there is a significant amount of molecular gas in the surrounding “envelope” regions around the filaments, to compare the ratio of Σ_{SMF} and $\Sigma_{^{13}\text{CO}}$ in the filaments we must first subtract the contribution to $\Sigma_{^{13}\text{CO}}$ from the envelopes. To do this we consider orthogonal strips across each IRDC filament and measure ^{13}CO emission on either side (see Figs. 3 & 4). The spectra of these “off-source”, envelope regions are corrected for optical depth effects, as described above, averaged and then subtracted from the central “on-source”, filament region (see Fig. 5). We find the envelope-subtracted

TABLE 1
ESCAPE PROBABILITIES AND CRITICAL DENSITIES

IRDC Spectrum (see Fig. 2)	$N_{^{13}\text{CO}}$ (10^{16} cm^{-2})	$\Sigma_{^{13}\text{CO}}$ (g cm^{-2})	β	n_{H_2} (cm^{-3})	βn_{crit} (cm^{-3})	$n_{\text{H}_2}/(\beta n_{\text{crit}})$
F _{mean}	2.73	0.0344	0.873	1340	1660	0.807
F _{high}	4.94	0.0622	0.705	2430	1340	1.81
H _{mean}	2.75	0.0347	0.696	2850	1322	2.15
H _{high}	3.46	0.0436	0.587	3590	1120	3.22

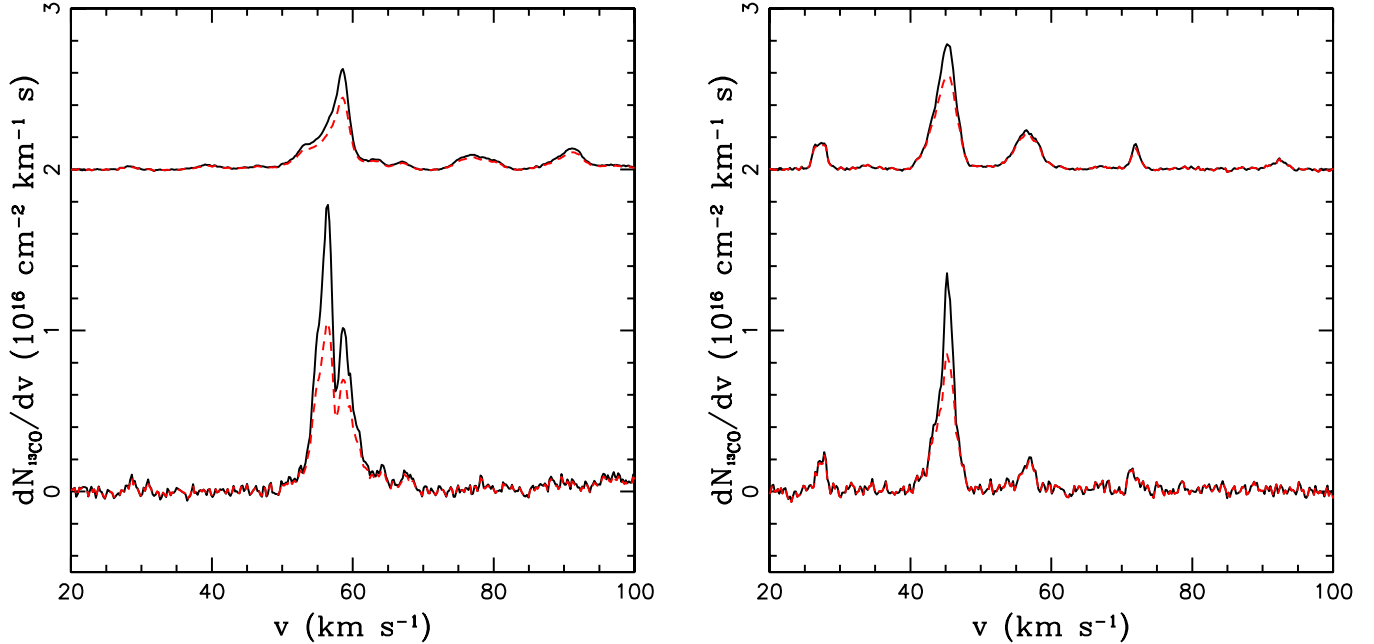


FIG. 2.— Column density profiles with velocity for IRDCs F (left) and H (right). The dashed lines shows the profiles assuming optically thin emission, while the solid lines show the profiles after correction for optical depth. A temperature of 20 K was assumed for IRDC F and 15 K for IRDC H (see text). For each cloud the upper, offset profile is that of the average for the cloud and the lower profile is that of the highest column density position.

spectra are generally narrower than the total. We also find that the size of negative residuals created in the subtraction process are relatively small. However, the fact that in some cases we see quite significant variation in the envelope spectra from one side of the filament to the other, suggests that this is one of the major sources of uncertainty in measuring the molecular emission properties of these embedded filaments. After this procedure, we are now in a position to compare the envelope-subtracted values of $\Sigma_{13\text{CO}}$ with those derived from the SMF extinction mapping method of BT09.

We also note that the MIR extinction derived values of Σ suffer from their own systematic uncertainties, including corrections due to foreground dust emission (BT09), scattering in the IRAC array (Battersby et al. 2010), adopted dust opacities and dust to gas ratios. However, saturation due to large $8\mu\text{m}$ optical depth and/or an insufficiently subtracted foreground is not an important source of error for our present study, since the values of Σ_{SMF} are in any case reduced when the maps are smoothed to the lower resolution of the ^{13}CO data.

As noted by BT09, the MIR extinction mapping technique fails for locations where there are bright MIR sources. If the intensity of the source is greater than the background model, then formally an unphysical, negative value of Σ is returned by this method. In the analysis of BT09, negative values of Σ are allowed up to a certain threshold value to account for noise-like, approximately Gaussian, fluctuations in the background intensity. For the more extreme fluctuations caused by bright sources, BT09 set $\Sigma = 0$. Thus the effect of a bright MIR region within an IRDC is to cause the extinction mapping method to underestimate the true mass surface density. For most point-like MIR sources, this effect is quite minor after the extinction maps are averaged to the $22.14''$ pixel scale of the CO observations. However, in IRDC F we identify two regions (indicated in Fig. 3), which are significantly affected by bright MIR sources and exclude them from the subsequent analysis.

The values of $\Sigma_{13\text{CO}}$ (after envelope subtraction) and Σ_{SMF} for each pixel in the filament regions of IRDCs F and H are compared in Figure 6. We note that both these measures of Σ are independent of the distance to the cloud. Considering just the data with $\Sigma_{13\text{CO}}$ and $\Sigma_{\text{SMF}} > 0.01 \text{ g cm}^{-2}$, the best fit power law relation $\Sigma_{13\text{CO}}/\text{g cm}^{-2} = A(\Sigma_{\text{SMF}}/\text{g cm}^{-2})^\alpha$ has $\alpha = 0.77 \pm 0.18, 0.32 \pm 0.28$ and $A = 0.58 \pm 0.44, 0.074 \pm 0.069$ for IRDCs F and H, respectively.

Over the range $0.01 < \Sigma_{\text{SMF}}/\text{g cm}^{-2} < 0.07$ we find that $\Sigma_{13\text{CO}} \simeq \Sigma_{\text{SMF}}$ to within a factor of ~ 2 for the mean values in each IRDC filament. The dispersion within an individual IRDC from pixel to pixel is also at about this level. The systematic offsets may reflect real systematic variations of the assumed temperature, ^{13}CO abundance, dust opacities or envelope subtraction method for each IRDC compared to our adopted values and methods. The dispersion may reflect local systematic variations and errors introduced by measurement noise.

In both IRDCs the ratio $\Sigma_{13\text{CO}}/\Sigma_{\text{SMF}}$ decreases with increasing mass surface density as measured by Σ_{SMF} . We gauge the significance of this trend by noting that the above values of α for IRDCs F and H differ from unity by 1.3 and 2.4 standard deviations, respectively, assuming errors are distributed normally.

There are several physical processes that may be causing such a trend. A systematic temperature decrease from the lower column density, outer regions of the filaments to the higher column density centers would lead us to systematically

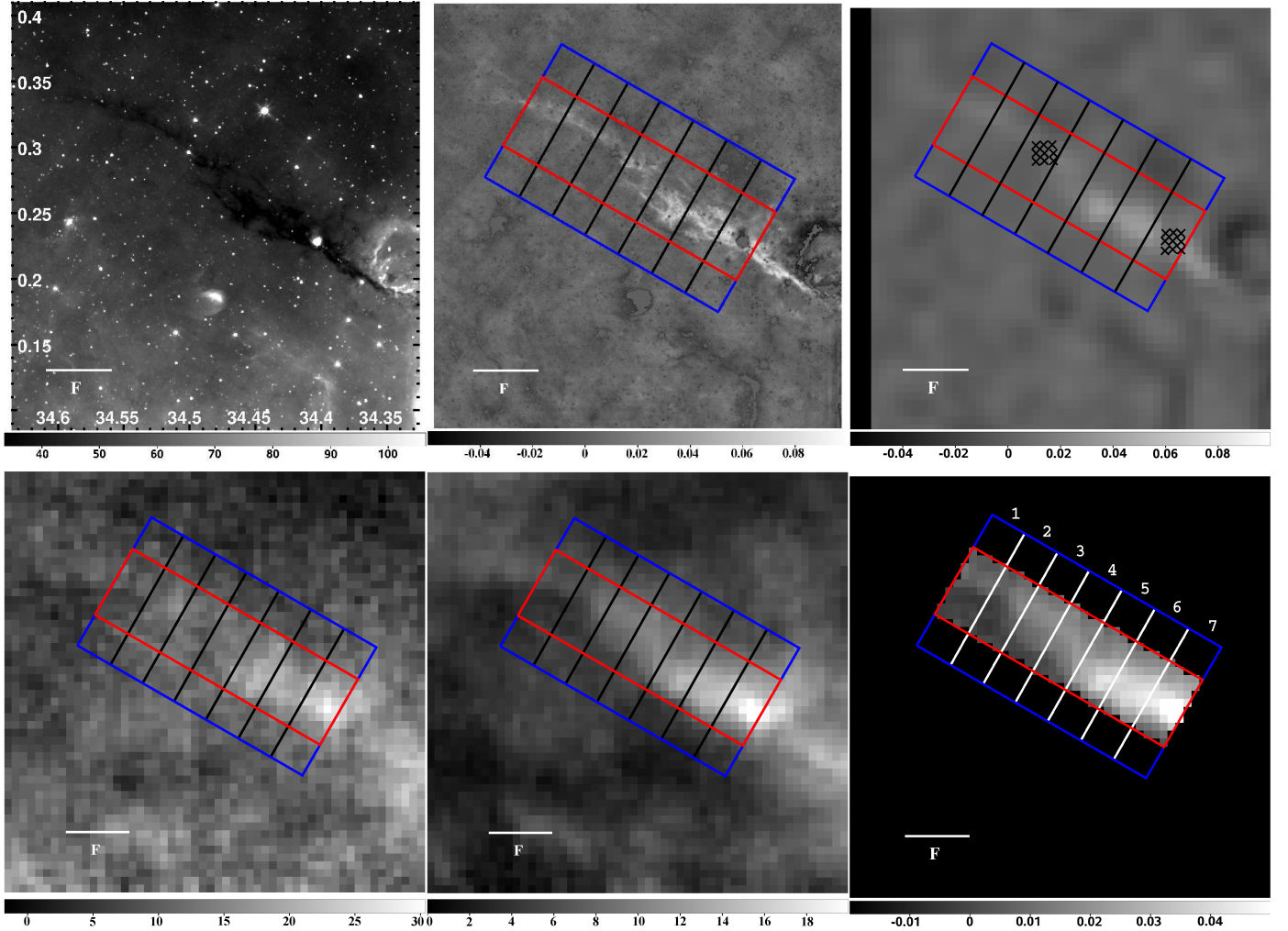


FIG. 3.— Morphology of IRDC F. *Top left*: *Spitzer* GLIMPSE IRAC $8\ \mu\text{m}$ image, with linear intensity scale in MJy sr^{-1} . The horizontal line shows a scale of $3'$. The image has $1.2''$ pixels and the PSF has a FWHM of $2''$. *Top middle*: Mass surface density, Σ_{SMF} , with linear intensity scale in g cm^{-2} , derived from the previous image using the small median filter MIR extinction mapping method of Butler & Tan (2009). The inner, red rectangle (centered at $l = 34.483^\circ$, $b = 0.276^\circ$, with P.A. = $+60^\circ$ and size 0.0582° by 0.198°) along the filament shows the “on source” region we consider to contain the main filamentary structure of the IRDC. The outer, blue rectangle extends to “off source” regions we consider to be representative of the surrounding GMC envelope. These rectangles are divided into 7 orthogonal strips to aid in the separation of components of CO emission from the filament and GMC envelope. *Top right*: The same extinction map convolved with a Gaussian of $46''$ FWHM to match the resolution of the CO maps and pixelated to $22''$ on the same grid as the GRS survey image. The two black hatched squares show regions with unreliable measures of Σ_{SMF} because of the presence of bright MIR sources. These are excluded from the comparison with $\Sigma_{13\text{CO}}$. *Bottom left*: Integrated intensity map of $^{13}\text{CO}(1-0)$ emission over the full velocity range of $-5 - 135\ \text{km s}^{-1}$ of the GRS survey, with linear intensity scale in K km s^{-1} . *Bottom middle*: Integrated intensity map of ^{13}CO over the velocity range of $48 - 65\ \text{km s}^{-1}$, i.e. the gas we believe is associated with the IRDC, with linear intensity scale in K km s^{-1} . *Bottom right*: Mass surface density of the filament derived from ^{13}CO emission, $\Sigma_{13\text{CO}}$, with linear intensity scale in g cm^{-2} .

underestimate $\Sigma_{13\text{CO}}$ in the latter, while having little direct effect on dust opacities (although there may be an indirect effect via formation of ice mantles, see below). For the temperature ranges we expect to be present, i.e. from $\sim 10\text{--}20\ \text{K}$ (e.g. Pillai et al. 2006 - although note these are based on measurements of NH_3 , which may trace different conditions to those of the ^{13}CO), this effect becomes important for values of $T_{B,\nu} \gtrsim 4\ \text{K}$ (see Fig. 1b). We illustrate the size of this effect for the highest Σ_{SMF} positions in IRDCs F and H in Fig. 6. A systematic temperature decrease of $5\ \text{K}$ in the high Σ regions could remove much of the observed trend.

Another possibility is that our corrections for the optical depth of the ^{13}CO emission are systematically underestimated at the higher column density positions. This would be expected if a significant amount of mass is contained in unresolved dense cores. The largest optical depth corrections in the highest column density positions presently lead to an increase in the estimated column by factors $\lesssim 2$. Future higher angular resolution ^{13}CO and C^{18}O observations of these filaments are required to investigate this issue further.

Depletion of CO molecules onto dust grains is known to occur in cold, high volume density gas (Caselli et al. 1999). This process could systematically reduce the gas phase CO abundance in the high Σ regions of the IRDCs. For depletion to be fully responsible for the observed trends in IRDCs F and H would require about a factor of 2 depletion as Σ_{SMF}

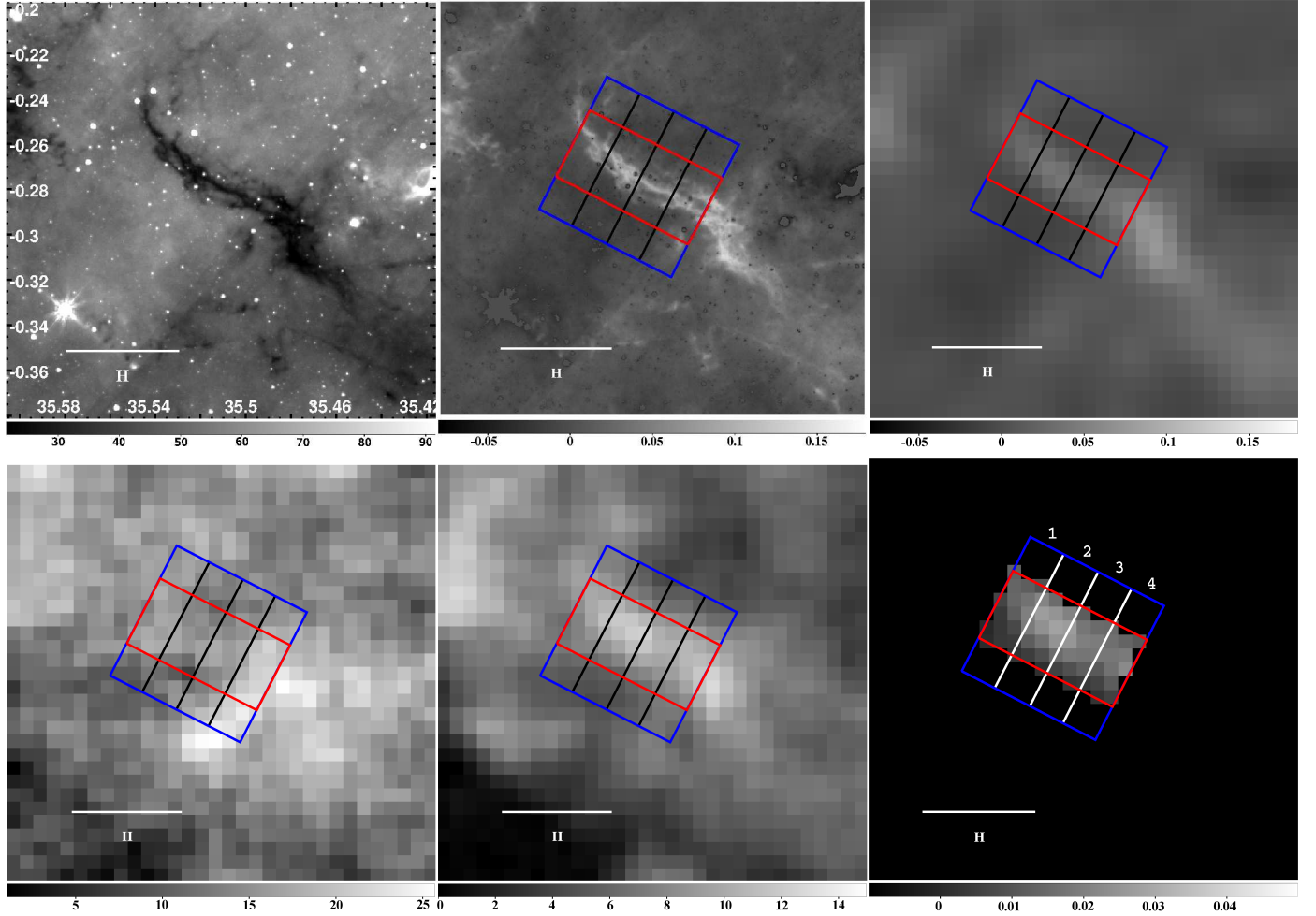


FIG. 4.— Morphology of IRDC H. *Top left*: *Spitzer* GLIMPSE IRAC $8\ \mu\text{m}$ image, with linear intensity scale in MJy sr^{-1} . The horizontal line shows a scale of $3'$. The image has $1.2''$ pixels and the PSF has a FWHM of $2''$. *Top middle*: Mass surface density, Σ_{SMF} , with linear intensity scale in g cm^{-2} , derived from the previous image using the small median filter MIR extinction mapping method of Butler & Tan (2009). The inner, red rectangle (centered at $l = 35.517^\circ$, $b = -0.275^\circ$, with P.A. = $+62.84^\circ$ and size $0.0307''$ by $0.0637''$) along the filament shows the “on source” region we consider to contain the main filamentary structure of the IRDC. The outer, blue rectangle extends to “off source” regions we consider to be representative of the surrounding GMC envelope. These rectangles are divided into 4 orthogonal strips to aid in the separation of components of CO emission from the filament and GMC envelope. *Top right*: The same extinction map convolved with a Gaussian of $46''$ FWHM to match the resolution of the CO maps and pixelated to $22''$ on the same grid as the GRS survey image. *Bottom left*: Integrated intensity map of ^{13}CO over the full velocity range of $-5 - 135\ \text{km s}^{-1}$ of the GRS survey, with linear intensity scale in K km s^{-1} . *Bottom middle*: Integrated intensity map of ^{13}CO over the velocity range of $40 - 50\ \text{km s}^{-1}$, i.e. the gas we believe is associated with the IRDC, with linear intensity scale in K km s^{-1} . *Bottom right*: Mass surface density of the filament derived from ^{13}CO emission, $\Sigma_{^{13}\text{CO}}$, with linear intensity scale in g cm^{-2} .

increases from 0.01 to $0.05\ \text{g cm}^{-2}$. Because of depletion, CO is not expected to be an ideal tracer of the densest, coldest parts of IRDCs. High resolution studies of other tracers, such as NH_3 , will likely be needed to measure the kinematics of these regions.

The depletion of CO via formation of CO ice mantles on dust grains would also have some effect on the MIR opacities of these grains, thus affecting our measurement of Σ_{SMF} . The grains would become larger and absorption features due to pre-existing water ice mantles may become obscured. The Ossenkopf & Henning (1994) grain models show a $\sim 50\%$ increase in $8\ \mu\text{m}$ opacity, $\kappa_{8\ \mu\text{m}}$, going from bare grains to those with thick ice mantles. The BT09 estimates of Σ_{SMF} assumed a constant value of $\kappa_{8\ \mu\text{m}}$ consistent with the thin ice mantle model of Ossenkopf & Henning (1994). Thus the observed decrease in the ratio of $\Sigma_{^{13}\text{CO}}/\Sigma_{\text{SMF}}$ with increasing mass surface density could be caused by thickening of grain ice mantles, causing us to systematically overestimate Σ_{SMF} .

Another possible explanation for a trend of decreasing $\Sigma_{^{13}\text{CO}}/\Sigma_{\text{SMF}}$ with increasing mass surface density is active chemical fractionation (Langer et al. 1980, 1984; Glassgold, Huggins, & Langer 1985; Visser, Van Dishoeck, & Black 2009), which enhances the abundance of ^{13}CO in regions where $^{13}\text{C}^+$ is present via the ion-molecule exchange

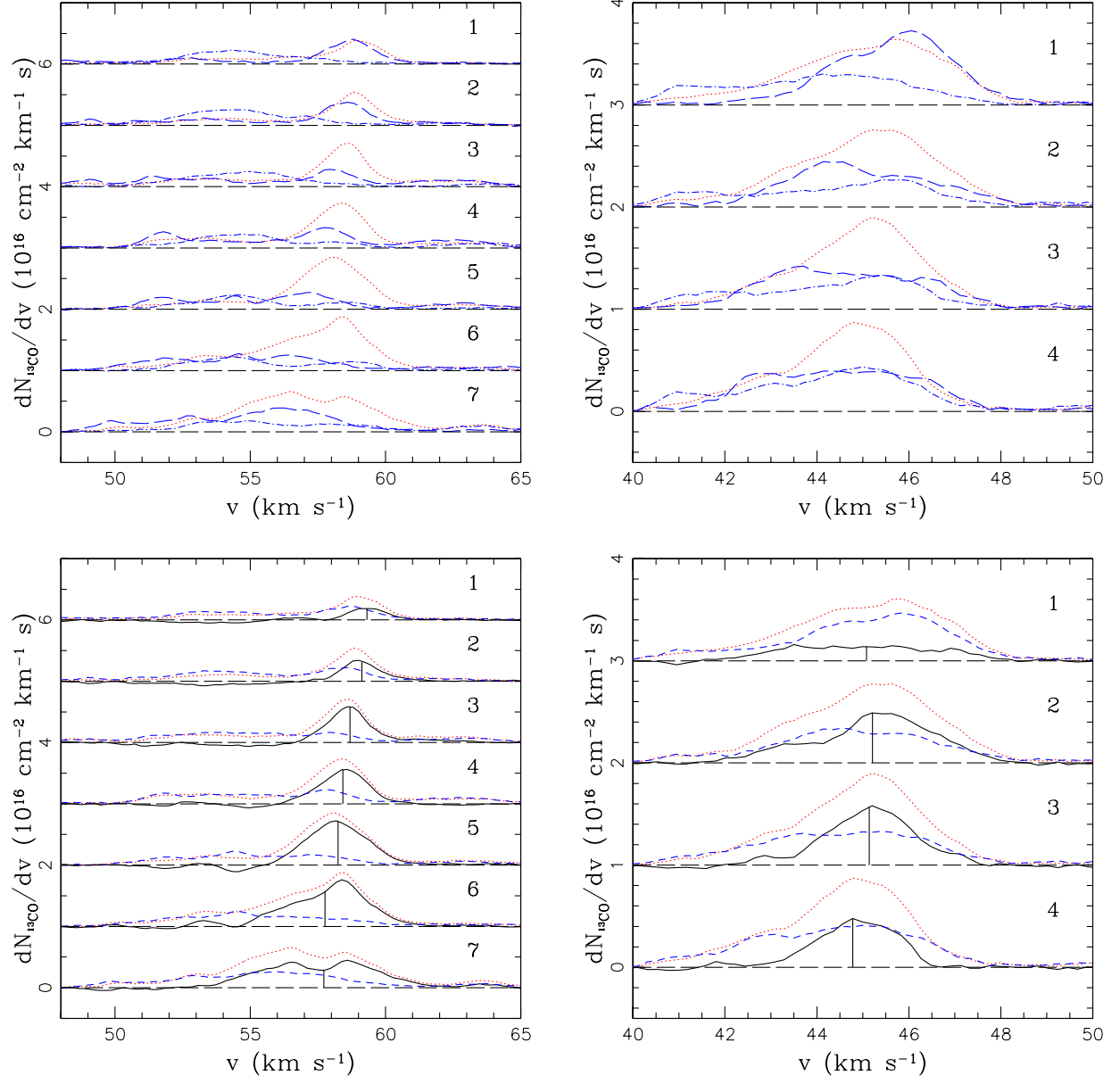


FIG. 5.— Subtraction of IRDC envelopes. (a) *Top left:* Filament and envelope of IRDC F, with the 7 sets of spectra (top to bottom) corresponding to the 7 orthogonal strips (top left to bottom right) shown in Figure 3. In each, the dotted, red line shows the total ^{13}CO column density distribution, including optical depth corrections, from the filament region, which includes an assumed contribution from "envelope" material along the line of sight. The long dashed and dot-dashed, blue lines show the total ^{13}CO column density from the northern and southern envelope regions, respectively. (b) *Top right:* Filament and envelope of IRDC H, with the 4 sets of spectra (top to bottom) corresponding to the 4 orthogonal strips (top left to bottom right) shown in Figure 4. The line styles have the same meaning as in (a). (c) *Bottom left:* For the same strips as in (a), we subtract the average of the northern and southern envelope spectra (short dashed blue lines) from the filament (dotted red line), to leave an estimate of the material in the filament (solid, black line). The vertical solid line indicates the mean velocity. (d) *Bottom right:* Same analysis and labels as (c) applied to IRDC H.

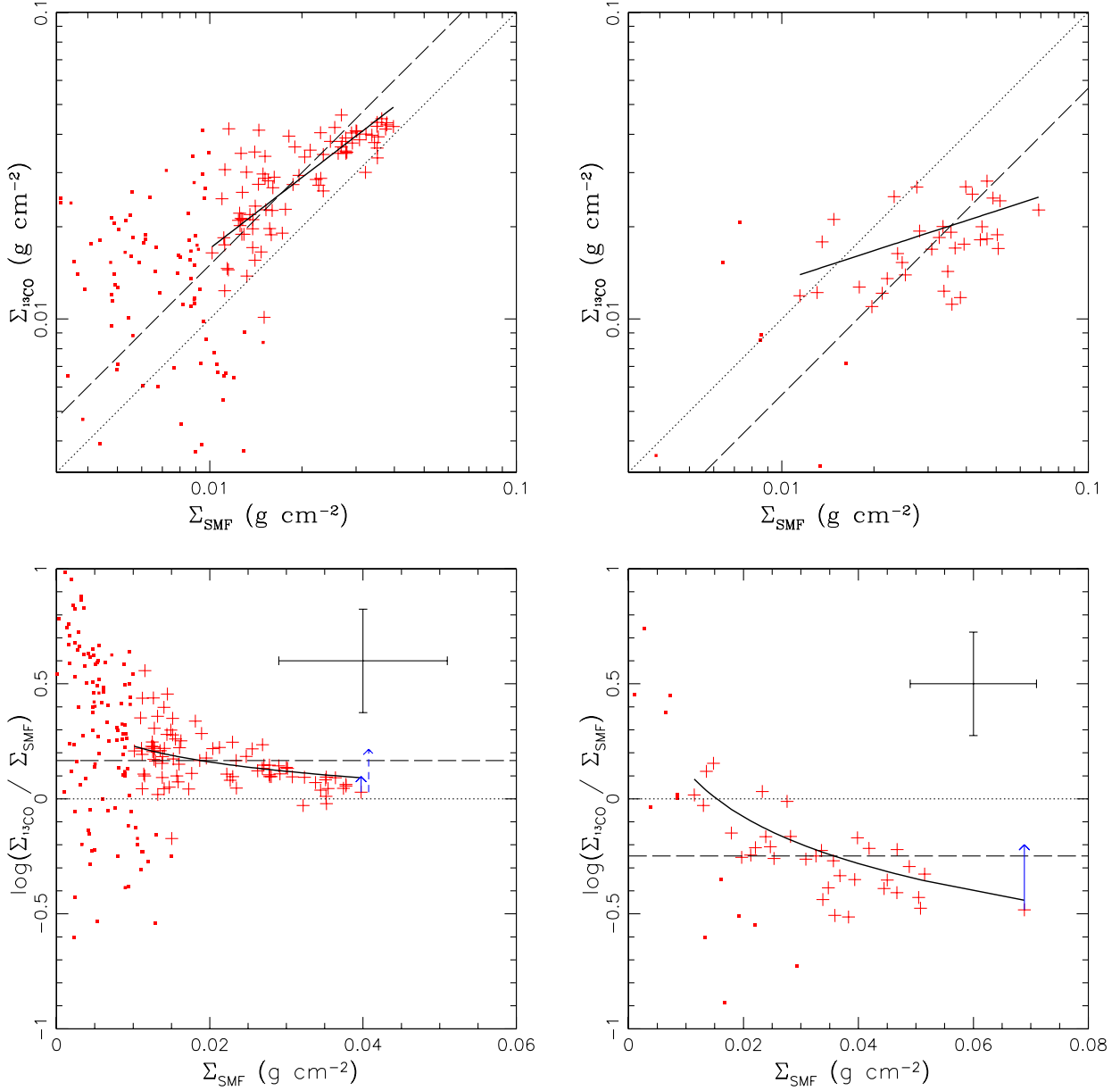


FIG. 6.— (a) *Top Left*: Direct comparison of $\Sigma_{13\text{CO}}$ (after envelope subtraction) and Σ_{SMF} in IRDC F. The crosses show locations where both $\Sigma_{13\text{CO}}$ and $\Sigma_{\text{SMF}} > 0.01 \text{ g cm}^{-2}$. The dots show locations of lower surface densities. The uncertainties in the individual measurements are assumed to be 15% plus a systematic error of 0.01 g cm^{-2} . The dotted line shows the one to one linear relation and the long dashed line shows the best-fit offset linear relation. The solid line shows the best-fit power law relation (see text). (b) *Top Right*: Same as (a) but for IRDC H. (c) *Bottom Left*: Logarithm of the ratio of $\Sigma_{13\text{CO}}$ to Σ_{SMF} as a function of Σ_{SMF} for IRDC F, with the same symbol notation as in (a). The cross in the upper-right corner indicates typical estimated uncertainties. The solid (dashed) arrow shows the effect on the highest Σ position of reducing the assumed temperature from 20 K to 15 K (10 K). (d) *Bottom Right*: Same as (c) but for IRDC H. The arrow shows the effect on the highest Σ position of reducing the assumed temperature from 15 K to 10 K.

reaction (Watson, Anicich, & Huntress 1976), $^{12}\text{CO} + ^{13}\text{C}^+ \rightarrow ^{12}\text{C}^+ + ^{13}\text{CO} + 35\text{K}$. FUV irradiation maintains a relatively high abundance of $^{13}\text{C}^+$ in the outer regions of the cloud, with $A_V \lesssim 1$ mag. The relative abundance of ^{13}CO to ^{12}CO can be enhanced by factors of ~ 10 . For $A_V \gtrsim 2$, the enhancement factor is only about 20% (e.g. for a model with $n_{\text{H}_2} = 10^3 \text{ cm}^{-3}$ and $T=20\text{ K}$; Glassgold et al. 1985). For IRDCs F and H, the filaments are typically embedded inside “envelope” gas with $\Sigma_{^{13}\text{CO}} \simeq 0.01 \text{ g cm}^{-2}$, i.e. $N_{\text{H}} \simeq 4 \times 10^{21} \text{ cm}^{-2}$. The trend of decreasing $\Sigma_{^{13}\text{CO}}/\Sigma_{\text{SMF}}$ is observed to occur as Σ_{SMF} increases to $\sim 0.05 \text{ g cm}^{-2}$. ^{13}CO fractionation enhancements should not be varying in this regime by large enough factors to explain our observed results. It should also be noted that even in the lower-column density regions, if the FUV flux is large enough, then isotope selective photodestruction of ^{13}CO compared to the self-shielded ^{12}CO (Bally & Langer 1982) may reverse the fractionation-produced enhancement of the abundance of ^{13}CO to ^{12}CO .

4. THE DYNAMICAL STATE OF THE IRDC FILAMENTS

4.1. IRDC Masses from ^{13}CO Emission and MIR Dust Absorption

We calculate IRDC masses using the observed mass surface densities and angular sizes, and by assuming near kinematic distances, since the clouds are seen in absorption against the Galaxy’s diffuse MIR emission. We adopt the kinematic distances of Simon et al. (2006), who assumed the Clemens (1985) rotation curve. This leads to a distance of 3.7 kpc for IRDC F and 2.9 kpc for IRDC H. We assume uncertainties of 0.5 kpc, which could result, for example, from line of sight noncircular motions of $\sim 8 \text{ km s}^{-1}$. Temperature uncertainties of 5 K would lead to $\Sigma_{^{13}\text{CO}}$ uncertainties of $\sim 20\%$. We estimate similar levels of uncertainty in Σ_{SMF} due to foreground correction and background interpolation uncertainties (BT09). Then, for IRDC F, the ^{13}CO -derived mass assuming $T = 20\text{ K}$ in the on-source filament region after envelope subtraction is $M_{^{13}\text{CO}} = 3300 \pm 1100 M_{\odot}$ and the dust extinction mass is $M_{\text{SMF}} = 1900 \pm 640 M_{\odot}$. For IRDC H, we find $M_{^{13}\text{CO}}(T = 15\text{ K}) = 370 \pm 150 M_{\odot}$ and $M_{\text{SMF}} = 580 \pm 230 M_{\odot}$. For our calculations involving the total mass of the clouds we take averages of the above estimates while still assuming 20% uncertainties in the averaged values of Σ . Thus we adopt $M = 2600 \pm 870 M_{\odot}$ for IRDC F and $M = 480 \pm 190 M_{\odot}$ for IRDC H. These results are summarized in Table 2.

4.2. Ellipsoidal Cloud Virial Analysis

Following Bertoldi & McKee (1992, hereafter BM92), we consider an ellipsoidal cloud with radius R normal to the axis of symmetry and size $2Z$ along the axis. The aspect ratio is defined as $y \equiv Z/R$, while R_{max} and R_{min} are the semimajor and semiminor axes of the ellipse obtained by projecting the cloud onto the plane of the sky.

IRDCs F and H both have relatively thin, filamentary morphologies: we set $R_{\text{max}}/R_{\text{min}} = 3.40, 1.78$, respectively, i.e. the same elongation as the rectangular regions we consider to define the filaments (Figs. 3 & 4). Given these morphologies, we expect the symmetry axes of the clouds to be close to the plane of the sky. Thus for both we adopt a fiducial value of the inclination angle between the cloud symmetry axis and the line of sight of $\theta = 60^\circ$. We assume $R = R_{\text{min}}$ and $Z = R_{\text{max}}/\sin\theta$, so $y = 3.93, 2.06$ for IRDCs F and H, respectively. An uncertainty of 15° in inclination would cause $\sim 15\%$ uncertainties in y . It is also useful to introduce a geometric mean observed radius, $R_{\text{obs}} \equiv (R_{\text{max}}R_{\text{min}})^{1/2}$, which is also related to R via, $R_{\text{obs}} = R\cos^{1/2}\theta[1 + (y\tan\theta)^2]^{1/4}$. BM92 also define R_m as the mean value of R_{obs} averaged over all viewing angles, but for our individual clouds we will express quantities in terms of R and R_{obs} . It should be noted that the treatment of these IRDC filaments as simple ellipsoids is necessarily approximate, and we consider the filamentary analysis of section 4.3 to be more accurate.

TABLE 2
IRDC ELLIPSOIDAL VIRIAL ANALYSIS

Cloud property	IRDC F	IRDC H
d (kpc)	3.7 ± 0.5	2.9 ± 0.5
R (pc)	1.88 ± 0.25	0.91 ± 0.16
R_{obs} (pc)	3.52 ± 0.48	1.21 ± 0.21
$y \equiv Z/R$	3.93 ± 0.6	2.06 ± 0.3
$\Sigma_{^{13}\text{CO}}$ (g cm^{-2})	0.0147 ± 0.003	0.0133 ± 0.003
Σ_{SMF} (g cm^{-2})	0.0082 ± 0.0016	0.0209 ± 0.004
$\Sigma_{^{13}\text{CO}}(\text{env})$ (g cm^{-2})	0.0196 ± 0.004	0.0212 ± 0.004
$M_{^{13}\text{CO}}$ (M_{\odot})	3300 ± 1100	370 ± 150
M_{SMF} (M_{\odot})	1900 ± 640	580 ± 230
M (M_{\odot})	2600 ± 870	480 ± 190
a_1	10/9	10/9
a_2	0.538	0.750
W (10^{46}erg)	-11.0 ± 7.1	-1.08 ± 0.78
σ (km/s)	1.46 ± 0.15	1.20 ± 0.12
$t_s = 2R/\sigma$ (Myr)	2.5 ± 0.4	1.5 ± 0.3
\mathcal{T} (10^{46}erg)	16.4 ± 6.4	2.06 ± 0.91
$\mathcal{T}_0(A)$ (10^{46}erg)	14 ± 8	2.7 ± 1.8
$\mathcal{T}_0(B)$ (10^{46}erg)	73 ± 30	4.3 ± 2.0
$\alpha \equiv 5\sigma^2 R/(GM)$	1.78 ± 0.73	3.17 ± 1.50

If the clump is in an environment that is evolving with a time scale longer than the clump's dynamical time scale or signal crossing time $t_s \equiv 2R/\sigma$, then it should obey the equilibrium virial equation (McKee & Zweibel 1992):

$$0 = 2(\mathcal{T} - \mathcal{T}_0) + \mathcal{M} + W. \quad (8)$$

Here, \mathcal{T} is the clump kinetic energy, \mathcal{T}_0 is the kinetic energy resulting from the surface pressure on the clump, \mathcal{M} is the magnetic energy associated with the cloud, and W is the gravitational binding energy, which for an ellipsoidal cloud is (BM92)

$$W = -\frac{3}{5}a_1a_2\frac{GM^2}{R}, \quad (9)$$

where for a power-law density distribution $\rho \propto r^{-k_\rho}$, $a_1 = (1 - k_\rho/3)/(1 - 2k_\rho/5)$ and

$$a_2 = \frac{\text{arcsinh}(y^2 - 1)^{1/2}}{(y^2 - 1)^{1/2}} \quad (10)$$

for prolate clouds. Note, our definition of W and a_2 differs slightly from BM92 since we do not need to consider R_m . We adopt $k_\rho = 1$ (based on a study of the density profiles in IRDCs - Butler & Tan, in prep.) so that $a_1 = 10/9$. For our measured values of y , we have $a_2 = 0.53, 0.71$ for IRDCs F and H, respectively. For the mass of the cloud we take the average values of the estimates from MIR dust extinction and ^{13}CO line emission. Using these values we estimate $W = -(11.0, 1.08) \times 10^{46}$ erg for IRDCs F and H, respectively (see Table 2). The uncertainties in W are relatively large given the measurement errors of Σ and R .

The clump kinetic energy is $\mathcal{T} = (3/2)M\sigma^2$, where σ is the average total 1D velocity dispersion, which we derive from the ^{13}CO line emission (counting only those parts of the envelope-subtracted spectra with positive signal greater than or equal to one standard deviation of the noise level) including corrections for the molecular weight of ^{13}CO and our adopted cloud temperatures. We estimate that we measure σ to a 10% accuracy. We find $\mathcal{T} = (16.4, 2.06) \times 10^{46}$ erg for IRDCs F and H, with uncertainties at about the 40% level.

The surface term for the kinetic energy is $\mathcal{T}_0 = (3/2)P_0V$. We estimate this term in two ways. First (method A), we can measure the mass surface density of the surrounding molecular cloud from the ^{13}CO emission of the envelope regions. We find $\Sigma_{^{13}\text{CO}}(\text{env}) = 0.0196, 0.0212 \text{ g cm}^{-2}$ for IRDCs F and H, respectively. We scale these values by $M/M_{^{13}\text{CO}}$, i.e. 0.79 and 1.30. If the envelope is self-gravitating, it has mean internal pressure $P(\text{env}) = 1.85G\Sigma^2(\text{env})$, adapting the analysis of McKee & Tan (2003) with parameters $f_g = 1$ (i.e. fully gas dominated), $\phi_{\text{geom}} \equiv R_{\text{obs}}^3/(R^2Z) = 1.4$ (adopting an intermediate value for the two IRDCs accurate to about 20%), $\phi_B = 2.8$ (the fiducial value of McKee & Tan, measuring the ratio of the total pressure including magnetic fields to that assuming they were absent) and $\alpha_{\text{vir}} = 1$. Thus setting $P_0 = P(\text{env}) = (2.96, 9.38) \times 10^{-11}$ cgs for IRDCs F and H and with the cloud volume $V = 4\pi R^2Z/3$, we find $\mathcal{T}_0(A) = (14, 2.7) \times 10^{46}$ erg.

Second (method B), we estimate the density in the envelope region, assuming it has a cylindrical, annular volume with outer radius $2R$ and inner radius R . For IRDCs F and H, we find densities of $\rho = 4\Sigma(\text{env})/(3\pi R) = (1.43, 3.20) \times 10^{-21} \text{ g cm}^{-3}$, equivalent to $n_{\text{H}}(\text{env}) = (610, 1600) \text{ cm}^{-3}$. We again scale these values by $M/M_{^{13}\text{CO}}$, i.e. 0.79 and 1.30 for IRDCs F and H, respectively. We then equate $P_0 = \rho(\text{env})\sigma^2(\text{env})$, where $\sigma(\text{env})$ is the velocity dispersion of the envelope gas (we find $3.65, 1.89 \text{ km s}^{-1}$ for IRDCs F and H) and evaluate $\mathcal{T}_0(B) = (3/2)VP_0 \rightarrow (73, 4.3) \times 10^{46}$ erg, with $V = (4/3)\pi R^2Z$.

These results indicate that, for both IRDCs, the surface pressure term of the virial equation is comparable to or much larger than the internal kinetic term, although the uncertainties are large. Assuming $\mathcal{T}_0 \geq \mathcal{T}$, then for virial equilibrium to be maintained would require $\mathcal{M} \equiv (1/8\pi) \int_{V_a} (B^2 - B_0^2) dV \geq -W$, where B_0 is the magnetic field strength far from the cloud and V_a is a volume that extends beyond the cloud where the field lines have been distorted by the cloud. Assuming V_a is the volume of the envelope regions and assuming negligible B_0 , we find $B \geq 10, 13 \mu\text{G}$ for IRDCs F and H. If a more realistic value of $B_0 = 10 \mu\text{G}$ is adopted (Crutcher et al. 2010), then we find $B \geq 14, 16 \mu\text{G}$. Thus relatively modest magnetic field enhancements could stabilize the clouds.

Bertoldi & McKee (1992) define a dimensionless virial parameter, $\alpha \equiv 5\sigma^2 R_m/(GM)$ to describe the dynamical state of clouds. We adopt a slightly revised definition $\alpha \equiv 5\sigma^2 R/(GM) = a_1 a_2 2\mathcal{T}/|W|$, with a_2 defined as above. For IRDCs F and H we find $\alpha = 1.78, 3.17$. While these values are quite close to unity, especially for IRDC F, which is commonly taken to infer that self-gravity is important, this is somewhat misleading since the value of a_2 is quite small for these elongated clouds and the surface pressure terms seem to be quite important.

It is possible that these IRDCs have not yet reached virial equilibrium if their surroundings are evolving on timescales $\lesssim t_s \sim$ a few Myr. The mean velocity of the ^{13}CO emitting gas in the north and south envelope regions is $55.72, 56.10 \text{ km s}^{-1}$, respectively, for IRDC F, and $44.96, 44.28 \text{ km s}^{-1}$, respectively, for IRDC H. The north/south velocity dispersions are $3.81/3.38 \text{ km s}^{-1}$ for F and $1.69/2.07 \text{ km s}^{-1}$ for H. The north/south $\Sigma_{^{13}\text{CO}}$'s are $0.040/0.031 \text{ g cm}^{-2}$ for F and $0.050/0.051 \text{ g cm}^{-2}$ for H. The ratios of north/south pressures (estimated by method B, $\propto \Sigma\sigma^2$) are thus 1.64 and 0.65 for IRDCs F and H. The pressures appear to be fairly similar on the different sides of the filaments, although the uncertainties are such that variation at the level of about a factor of two could be present.

4.3. Filamentary Cloud Virial Analysis

Fiege & Pudritz (2000, hereafter FP00) present a virial analysis of filamentary clouds. They derived the following equation satisfied by pressure-confined, nonrotating, self-gravitating, filamentary (i.e. lengths \gg widths) clouds threaded by helical magnetic fields that are in virial equilibrium:

$$\frac{P_0}{P} = 1 - \frac{m}{m_{\text{vir}}} \left(1 - \frac{\mathcal{M}_l}{|W_l|} \right). \quad (11)$$

Here P_0 is the external pressure at the surface of the filament, $P = \rho\sigma^2$ is the average total pressure in the filament, m is the mass per unit length, $m_{\text{vir}} \equiv 2\sigma^2/G$ is the virial mass per unit length, \mathcal{M}_l is the magnetic energy per unit length, and $W_l = -m^2G$ is the gravitational energy per unit length.

We divide IRDCs F, H into 7, 4 orthogonal strips (see Figs. 3 & 4) with angular widths $1.70'$, $0.955'$ along the filaments, respectively. Assuming a fiducial value of the inclination angle between the cloud symmetry axis and the line of sight of $\theta = 60^\circ$, these correspond to physical lengths along the filaments of 2.11, 0.930 pc, respectively.

In Table 3, for each strip in IRDCs F and H, we list the values of $\Sigma_{13\text{CO}}$, Σ_{SMF} , M (calculated from the mean of these values of Σ), m , ρ , \bar{v} , σ , m_{vir} , P , $\Sigma_{13\text{CO}}(\text{env})$, $\rho(\text{env})$ (calculated after scaling $\Sigma_{13\text{CO}}(\text{env})$ by $0.5(\Sigma_{13\text{CO}} + \Sigma_{\text{SMF}})/\Sigma_{13\text{CO}}$), $\bar{v}(\text{env})$, $\sigma(\text{env})$ and $P(\text{env}) \equiv \rho(\text{env})\sigma^2(\text{env})$. We equate $P_0 = P(\text{env})$.

Following FP00, in Fig. 7 we plot P_0/P versus m/m_{vir} . The range of models considered by FP00 allows for positive values of $\mathcal{M}_l/|W_l|$ (i.e. poloidally-dominated B-fields that provide net support to the filament against gravitational collapse) and negative values (i.e. toroidally-dominated B-fields that provide net confinement of the filament). In all cases, $P_0/P \leq 1$. In contrast, we find all of the filament regions have $P_0/P > 1$, i.e. the pressures in the envelope regions appear to be greater than in the filament. This echoes the results from the ellipsoidal virial analysis, which found large surface pressure terms. Assuming our measurements of pressures are reliable, e.g. are not being adversely affected by systematic effects due to, for example, our assumed filament and envelope geometry, then these results imply that the filaments have not yet reached virial equilibrium.

Very large values of P_0/P are inferred for strips F1, F2 and F3. These are consistent with the filament and envelope spectra shown in Fig. 5, which reveal a relatively weak filament and relatively strong and varying envelope velocity profiles.

Strips F6, F7 and H2 have the smallest values of $P_0/P \lesssim 2$. Examining the IRAC $8\mu\text{m}$ images (Figs. 3 & 4), there is some indication that these are the sites of relatively active star formation (especially F7 and H2). Star formation requires gravitationally unstable conditions in the filament, i.e. regions where self-gravity starts to dominate over external pressure. Our results indicate that this also requires the local region of the filament to reach approximate virial equilibrium, although surface pressure terms still remain dynamically important, i.e. m/m_{vir} is significantly less than unity. Given our measurement uncertainties and the fact that the observed regions do not have $P_0/P < 1$, we are not able to determine whether the field geometries are more dominated by poloidal or toroidal components. We note that FP00's conclusion that observed filaments are dominated by toroidal fields depends on their assumption that the filaments are in virial equilibrium and on their choice of P_0 , which was not directly measured for most of the sources they considered.

We caution that if independent molecular clouds are present along these lines of sight and with similar velocities to the filaments, then this may cause us to overestimate the velocity dispersion and pressure in the envelope regions around the filaments. From the spectra shown in Fig. 5 we do not expect this is occurring in IRDC H, since the envelope spectra share a very similar velocity range as the filament. The situation in IRDC F is less clear cut, since there appears to be a broader, offset component that dominates more in the envelope region.

5. CONCLUSIONS

We have compared measurements of mass surface density, Σ , in two IRDC filaments based on ^{13}CO observations, $\Sigma_{13\text{CO}}$, with those derived from MIR extinction mapping, Σ_{SMF} , finding agreement at the factor of ~ 2 level. A systematic decrease

TABLE 3
IRDC FILAMENTARY VIRIAL ANALYSIS

Cloud property	F1	F2	F3	F4	F5	F6	F7	F _{tot}	H1	H2	H3	H4	H _{tot}
$\Sigma_{13\text{CO}}$ ($10^{-2} \text{ g cm}^{-2}$)	0.218	0.338	0.811	1.31	2.29	2.87	2.58	1.47	0.864	1.67	1.56	1.21	1.33
Σ_{SMF} ($10^{-2} \text{ g cm}^{-2}$)	0.476	0.311	-0.0432	0.862	1.37	1.62	1.03	0.823	1.38	1.94	1.97	3.28	2.09
M (M_\odot)	114	107	126	357	601	737	593	2640	78.5	126	124	157	478
m ($M_\odot \text{ pc}^{-1}$)	54.0	50.7	59.7	169	285	349	281	178	84.4	135	133	169	128
ρ ($10^{-22} \text{ g cm}^{-3}$)	3.29	3.09	3.64	10.3	17.4	21.3	17.1	10.9	22.0	35.1	34.6	44.0	33.3
\bar{v} (km s^{-1})	59.19	59.34	58.81	58.26	58.30	57.77	57.77	58.39	45.09	45.20	45.13	44.78	45.07
σ (km s^{-1})	1.36	1.27	1.07	1.44	1.59	1.86	2.27	1.46	1.52	1.34	1.03	0.995	1.20
m_{vir} ($M_\odot \text{ pc}^{-1}$)	856	751	536	962	1170	1610	2400	986	1070	840	494	460	669
P (10^{-12} cgs)	6.05	4.99	4.19	21.3	43.8	73.8	88.3	23.1	50.7	63.4	36.8	43.6	47.9
$\Sigma_{13\text{CO}}(\text{env})$ ($10^{-2} \text{ g cm}^{-2}$)	1.61	1.83	1.94	2.14	1.81	1.95	2.46	1.96	2.31	1.86	2.00	2.35	2.12
$\rho(\text{env})$ ($10^{-22} \text{ g cm}^{-3}$)	18.7	12.9	6.72	13.0	10.6	11.2	12.6	11.2	45.3	30.4	34.2	65.9	41.2
$\bar{v}(\text{env})$ (km s^{-1})	56.03	55.84	55.78	56.59	56.04	55.65	55.72	55.95	44.97	44.78	44.53	44.40	44.67
$\sigma(\text{env})$ (km s^{-1})	3.45	3.48	3.95	3.91	3.55	3.43	3.56	3.65	1.85	1.91	1.89	1.86	1.89
$P(\text{env})$ (10^{-12} cgs)	223	156	105	199	133	132	159	149	155	110	122	229	148

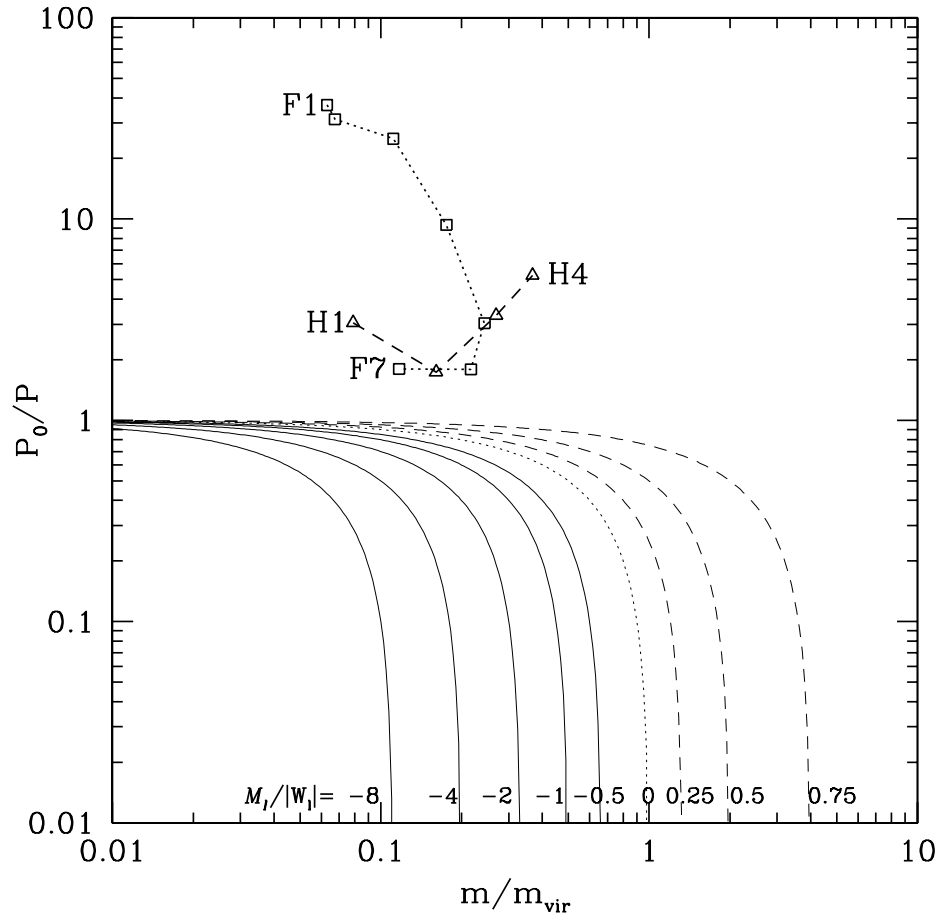


FIG. 7.— P_0/P versus m/m_{vir} for strips in IRDCs F (open squares joined by dotted line for F1 to F7) and H (open triangles joined by dashed line for H1 to H4). The smooth curves show the conditions satisfied by equation (11) for $\mathcal{M}_t/|W_t| < 0$ (solid lines), $\mathcal{M}_t/|W_t| = 0$ (dotted line), and $\mathcal{M}_t/|W_t| > 0$ (dashed lines). The large observed values of P_0/P may indicate that most of the regions in IRDCs F and H have not yet established virial equilibrium. Those strips with the lowest values of P_0/P , i.e. F6, F7, and H2, appear to be undergoing more active star formation (see text and Figs. 3 & 4).

in $\Sigma_{13\text{CO}}/\Sigma_{\text{SMF}}$ with increasing Σ may be due to a systematic decrease in temperature, increase in the contribution of under-resolved high optical depth regions, increase in dust opacity, or decrease in ^{13}CO abundance due to depletion in regions of higher column density. Future studies that spatially resolve the temperature structure and MIR dust absorption properties can help to distinguish these possibilities.

We have then used the kinematic information derived from ^{13}CO to study the dynamical state of the IRDCs. In particular we have evaluated the terms of the steady-state virial equation, including surface terms, under the assumption of ellipsoidal and filamentary geometries. In both cases we find evidence that the surface pressure terms are important and possibly dominant, which may indicate that the filaments, at least globally, have not yet reached virial equilibrium.

These results would be consistent with models of compression of dense gas in colliding molecular flows, e.g. GMC collisions. Tan (2000) proposed that this mechanism may trigger the majority of star formation in shearing disk galaxies. The expected collision velocities are $\sim 10 \text{ km s}^{-1}$. It is less clear whether colliding atomic flows, (e.g. Heitsch et al. 2008), which form the molecular gas after shock compression of atomic gas, would also produce such kinematic signatures: recall that we are inferring large surface pressures based on ^{13}CO emission from the envelopes around the IRDC filaments.

Recent observations of extended, parsec-scale SiO emission, likely produced in shocks with velocities $\gtrsim 12 \text{ km s}^{-1}$ in IRDC H by Jiménez-Serra et al. (2010) may also support models of filament formation from converging flows. However, we caution that the observed extended SiO emission is very weak and may also be produced by multiple protostellar outflow sources forming in the IRDC (see Jiménez-Serra et al. 2010 for further discussion).

Our resolved filamentary virial analysis also indicates that the regions closest to virial equilibrium (strips F6, F7 and H2) are those which have initiated the most active star formation. This would be expected if models of slow, equilibrium star formation (Tan et al. 2006; Krumholz & Tan 2007) apply locally in these regions. In this case, these dense regions that have become gravitationally unstable, perhaps due to the action of external pressure and/or converging flows, then persist for more than one local dynamical time and so are able to reach approximate pressure and virial equilibrium with their surroundings. In this scenario, they are stabilized by the ram pressure generated by protostellar outflow feedback from the forming stars (Nakamura & Li 2007).

We thank Michael Butler for providing the MIR extinction maps used in this analysis. We also thank Peter Barnes, Crystal Brogan, Michael Butler, Paola Caselli, James Jackson, Izaskun Jiménez-Serra, Thushara Pillai and Robert Simon for helpful discussions. The comments of an anonymous referee led to improvements in the paper. AKH acknowledges support from a SEAGEP Dissertation Fellowship. JCT acknowledges support from NSF CAREER grant AST-0645412 and NASA Astrophysics Theory and Fundamental Physics grant ATP09-0094.

REFERENCES

- Battersby, C., Bally, J., Jackson, J. M. et al. 2010, *ApJ*, 721, 222
 Bally, J., & Langer, W. D. 1982, *ApJ*, 255, 153
 Bertoldi, F., & McKee, C. F. 1992, *ApJ*, 395, 140 (BM92)
 Butler M. J., & Tan J. C. 2009, *ApJ*, 696, 484 (BT09)
 Carey, S. J., Clark, F. O., Egan, M. P., Price, S. D., Shipman, R. F., & Kuchar, T. A. 1998, *ApJ*, 508, 721
 Carey, S. J., Feldman, P. A., Redman, R. O., Egan, M. P., MacLeod, J. M., & Price, S. D. 2000, *ApJ*, 508, 721
 Caselli, P., Walmsley, C. M., Tafalla, M., Dore, L., & Myers, P. C. 1999, *ApJ*, 523, L165
 Clemens, D. P. 1985, *ApJ*, 295, 422
 Crutcher, R. M., Wandelt, B., & Falgarone, E. 2010, in *From Stars to Galaxies*, J. Tan & S. Van Loo (eds.), e-proceedings: <http://conference.astro.ufl.edu/STARSTOGALAXIES/>, p3
 Devine, K. (2009), Ph.D. Thesis, University of Wisconsin
 Fiege, J. D., & Pudritz, R. E. 2000, *MNRAS*, 311, 85 (FP00)
 Glassgold, A. E., Huggins, P. J., & Langer, W. D. 1985, *ApJ*, 290, 615
 Goodman A. A., Pineda J. E., Schnee, S. L. 2009, *ApJ*, 692, 91
 Heitsch, F., Hartmann, L. W., Slyz, A. D., Devriendt, J. E. G., & Burkert, A. 2008, *ApJ*, 674, 316
 Heyer, M. H., Krawczyk, C., Duval, J., & Jackson, J. M. 2009, *ApJ*, 699, 1092
 Jackson, J. M., Rathborne, J. M., Shah, R. Y. et al. 2006, *ApJS*, 163, 145
 Jiménez-Serra, I., Caselli, P., Tan, J. C., Hernandez, A. K., Fontani, F., Butler, M. J., & Van Loo, S. 2010, *MNRAS*, 406, 187
 Krumholz, M. R., & Tan, J. C. 2007, *ApJ*, 654, 304
 Lacy, J. H.; Knacke, R.; Geballe, T. R.; Tokunaga, A. T. 1994, *ApJ*, 428, L69
 Langer, W. D., Goldsmith, P. F., Carlson, E. R., & Wilson, R.W. 1980, *ApJ*, 235, L39
 Langer, W. D., Graedel, T. E., Frerking, M. A., & Armentrout, P. B. 1984, *ApJ*, 277, 581
 McKee, C. F., & Tan, J. C. 2003, *ApJ*, 585, 850
 McKee, C. F., & Zweibel, E. G. 1992, *ApJ*, 399, 551
 Milam, S. N., Savage, C., Brewster, M. A., & Ziurys, L. M., 2005, *ApJ*, 634, 1126
 Ossenkopf, V., & Henning, T. 1994, *A&A*, 291, 943
 Nakamura, F. & Li, Z.-Y. 2007, *ApJ*, 662, 395
 Pillai, T., Wyrowski, F., Carey, S. J., & Menten 2006, *A&A*, 450, 569
 Pineda, J. E., Caselli, P., & Goodman, A. A. 2008, *ApJ*, 679, 481
 Rathborne, J. M., Jackson, J. M., & Simon, R. 2006, *ApJ*, 641, 389
 Simon, R., Rathborne, J. M., Shah, R. Y., Jackson, J. M., & Chambers, E. T. 2006, *ApJ*, 653, 1325
 Tan, J. C. 2000, *ApJ*, 536, 173
 Tan, J. C. 2007, in *Triggered Star Formation in a Turbulent ISM*, eds. B. G. Elmegreen & J. Palous, IAUS 237, CUP, p258
 Tan, J. C., Krumholz, M. R., McKee, C. F. 2006, *ApJ*, 641, L121
 Visser, R., van Dishoeck, E. F., & Black, J. H., 2009, *A&A*, 503, 323
 Watson, W. D., Anicich, V. G., & Huntress, W. T., Jr. 1976, 205, L165